PROCEEDINGS OF SPIE

SPIEDigitalLibrary.org/conference-proceedings-of-spie

Integration and evaluation of a near-infrared camera utilizing a HgCdTe NICMOS3 array for the Mt. Palomar 200-inch Observatory

Carlos R. Jorquera, Charles A. Beichman, Carl F. Bruce, Thomas Nicholas Gautier, Thomas C. Jarrett

Carlos R. Jorquera, Charles A. Beichman, Carl F. Bruce, Thomas Nicholas Gautier, Thomas C. Jarrett, "Integration and evaluation of a near-infrared camera utilizing a HgCdTe NICMOS3 array for the Mt. Palomar 200-inch Observatory," Proc. SPIE 1946, Infrared Detectors and Instrumentation, (20 October 1993); doi: 10.1117/12.158705

SPIE.

Event: Optical Engineering and Photonics in Aerospace Sensing, 1993, Orlando, FL, United States

Integration and evaluation of a near infrared camera utilizing a HgCdTe NICMOS3 array for the Mt. Palomar 200-inch Observatory

Carlos Jorquera, Charles Beichman, Carl Bruce, Nick Gautier, Tom Jarrett

Jet Propulsion Laboratory, California Institute of Technology
Mail Stop 303-210, 4800 Oak Grove Drive
Pasadena, CA 91109

ABSTRACT

In this paper we describe the main subsystems that constitute the Mt. Palomar Prime Focus InfraRed Camera (PFIRCAM), together with some of the characterization data obtained for the focal plane array. This camera is currently a facility instrument at the 200-inch Mt. Palomar Observatory. It helps to satisfy the observational needs of astronomers in the spectral range of 1 μm to 2.5 μm by utilizing a HgCdTe NICMOS3 array. The camera has a plate scale of 0.54 arcsec/pixel for an overall FOV of 138 x 138 arcsec.

1. INTRODUCTION

One of the latest upgrades to the PFIRCAM has involved replacing the old focal plane array with a NICMOS3 array. The camera had been using the NICMOS2 array, the predecessor to the NICMOS3, which has a smaller pixel format of 128 x 128 pixels. This earlier camera configuration has been discussed in a previous paper[1]. The many advantages of using the NICMOS3 array include a larger FOV while at the same time allowing for an improved spatial resolution due to the smaller pixel size. Furthermore, various modifications to the detector design by the manufacturer have resulted in an overall better performing array, in particular having lower read noise and improved cosmetic qualities. In what follows we describe the main subsystems of the camera including the focal plane array, the dewar and optics, the data acquisition and timing electronics, and the acquisition-control and analysis software used at the laboratory for system characterization. In addition we present some of the data obtained in characterizing the array. We then conclude with some of the astronomical images that have been obtained with this camera.

2. PFIRCAM SYSTEM DESCRIPTION

The focal plane array and camera optics are enclosed in a fairly large cylindrical dewar which mounts to the prime focus pedestal of the 200-inch Observatory. The data acquisition, transmission, timing, and bias electronics attach directly to the outside of the dewar as a single unit. The power supplies for these electronics also reside at the prime focus cage, but are housed in a separate unit which connects to the camera electronics via shielded cables. Image data is transmitted through a pair of coaxial cables to a high speed data receiver located near the controller PC. The receiver then transmits the data to a buffer/processor board located at the PC bus. At the telescope, the PC serves as a slave waiting for commands from the telescope computer from which observation runs are controlled. The telescope computer specifies the parameters for an observation sequence to the PC which then controls the camera through another board in its bus. Once a set of images are collected and coadded, the PC writes the resulting image to common storage. At this point other computer systems at the telescope are able to access the data. At the laboratory, the PC not only serves as the control computer but also as the data analysis system. For this purpose we have developed an extensive software package which allows for detailed analysis and characterization of the camera.

2.1. The focal plane array (FPA)

The near-infrared detector used in the camera is a NICMOS3 device developed by Rockwell International under a NASA-funded contract through the University of Arizona[2]. It is a backside-illuminated 256 x 256-pixel hybrid focal plane array. The detector material is liquid phase epitaxy (LPE) HgCdTe grown on a sapphire substrate. The photodiode detector array is formed by ion implantation into the HgCdTe layer. The resulting pixel size is 40 μm x 40μm. The band gap of the photovoltaic detectors is tuned to a 2.5 μm cutoff wavelength by choosing the appropriate concentrations of Cd and Hg[3].

 0-8194-1182-5/93/$6.00

The detector array is cold welded to a Silicon multiplexer readout through indium columns. The readout is divided into four electrically isolated quadrants, each one consisting of a CMOS FET-switch array having its own output amplifier. The multiplexer unit cell architecture follows the principle of a source-follower-per-detector, which means that the detector photodiodes are connected directly to the gate of a switched source follower amplifier. Fig. 1 is a functional schematic for one quadrant of the array highlighting the unit cell architecture. Please refer to this figure for the following operational description.

The array is operated by first resetting the cathode of the photodiode to DET BIAS, so as to reverse bias the detector to about 0.5 V. This is accomplished by the actuation of MOSFETs M2 and M4. Once reset FET M2 is off, the cathode of the detector is left floating. Photocurrent and dark current are then integrated into the capacitance of the integration node. This capacitance is the sum of MOSFET M1's gate capacitance, the photodiode reverse-bias capacitance, and the stray capacitances due to the layout geometry. After a user-defined integration time has elapsed, the voltage at the unit cell source follower is sampled at the output amplifier M7 (which is also a source follower) by turning M3 and the row select on.

Each pixel of the array is sequentially read out in this manner via the action of CMOS shift registers, which supply the column and row select clock pulses. Various multiplexing schemes are configurable with slight timing variations. The nominal timing configuration sequentially resets each pixel, integrates for a pre-selected time, and then sequentially reads each pixel. In this way, the integration time seen by each pixel in one particular quadrant is of identical duration but shifted in time by one pixel clock period. This has the effect of defining the minimum integration time possible per quadrant as the product of the number of pixels in one quadrant and the pixel rate. For a nominal pixel rate of 250 KHz, the minimum quadrant read out time is 0.066 sec. Since for our configuration the four quadrants are read out sequentially, the minimum integration time for the whole array is 0.262 sec.

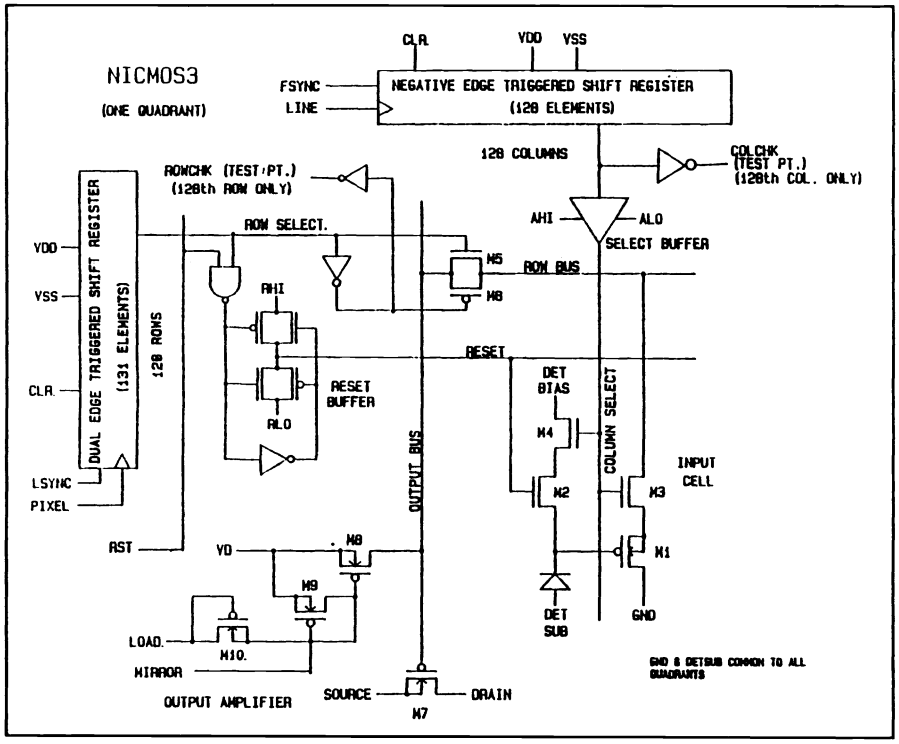

Figure 1. NICMOS3 array functional schematic.

2.2. The camera dewar and optics

The NICMOS3 array and associated optics are housed in an Infrared Laboratories HD-8 cylindrical dewar which is approximately two feet tall and has a diameter of 9 inches. The dewar features two liquid nitrogen vessels: the outer one

cools the radiation shield while the inner one maintains the NICMOS3 array and optics at the 77 K operating temperature. The hold time for the dewar is approximately 20 hours.

The dewar bolts directly to the prime focus pedestal of the 200 inch Telescope, looking down at the primary mirror. There are two optical subsystems within the dewar (Fig. 2). Light first passes through a pair of CaF_2 lenses that serve as a modified Ross corrector[4] to remove residual coma from the image formed by the parabolic 200-inch primary mirror. Chromatic aberrations due to this lens pair are minimized because of the lenses' low magnification.

Two filter wheels follow the Ross corrector, each containing eight filter positions. Each wheel has one open and one blank-off plate for dark current measurements. The thirteen remaining positions contain a number of broad- and narrow-band filters for the 1 to 2.5 μm region. The broad-band photometric filters include J, H, and K (1.25, 1.65, and 2.2 μm, respectively), while the narrow-band filters having 1% to 3% fractional bandwidths are centered on specific spectral lines including H_2 (2.12 and 2.24 μm), Brackett gamma (2.16 μm), and FeII (1.64 μm).

After passing through this pair of filter wheels, the light enters an Offner relay, which re-images the image formed by the 200-inch primary mirror on a cold stop that rejects background radiation from the telescope. The primary of the Offner relay is Zerodin glass; the secondary of the Offner is a diamond-turned aluminum mirror with a slightly aspheric surface. A hole in the Offner secondary matches the hole in the 200-inch primary. Finally, the light is folded once and imaged onto the NICMOS3 array.

The parameters of the optical system were optimized using Code V, and the system performance is quite good. The 256 x 256 pixel NICMOS3 array has 40 μm pixels that result in a plate scale of 0.54 arcsec / pixel and a 138 x 138 arcsec field of view. Images at the center of the field are usually limited by the seeing at Palomar. There is some residual coma at the edges of the field.

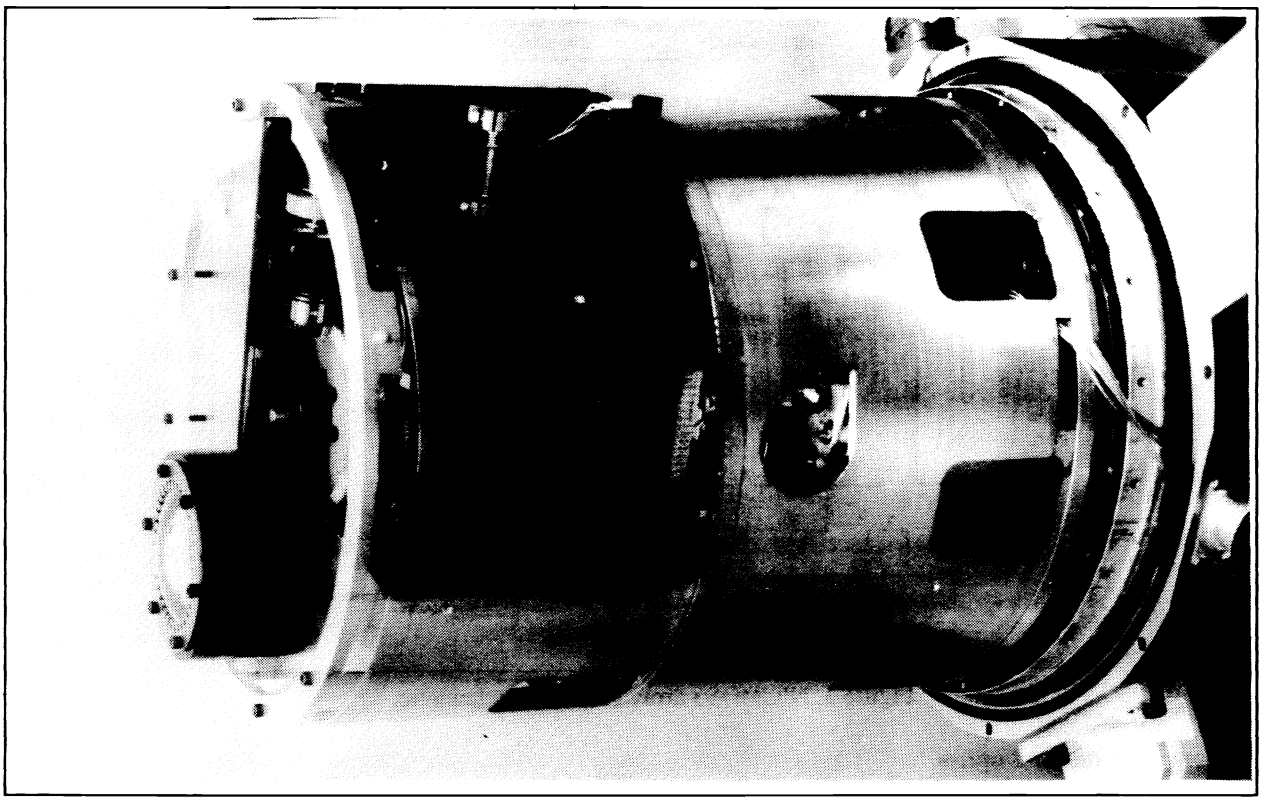

Figure 2. Illustration of the camera with its outer jacket and inner shield removed. Most optical components can be seen.

2.3. The electrical interface

The NICMOS3 readout is a 256 x 256 unit cell device which is divided into quadrants of 128 x 128 unit cells. These quadrants are electrically independent with the exception of Vss and DETSUB. The array was divided into quadrants for reasons particular to the NICMOS Project and do not represent any fundamental constraints.

Each quadrant has 5 clocks: FSYNC, LINE, RST, CLR, LSYNC and PIXEL. Each of these clocks passes through a 100 Ohm resistor which is located on the focal plane circuit card and then branches off in parallel to each of the quadrant clock inputs, with the exception of FSYNC which is unique to each quadrant. These clock lines are unshielded constantan wire. Shielding was not believed to be necessary due to the low frequency (<400 KHz) nature of the device.

Vss is a single point ground for the focal plane circuit card and it returns to the clock interface and bias board which share a common ground plane with the preamplifiers and the ADC. All device grounds or low points are tied to Vss at a single point. Copper wire is used for this node to minimize shifts in the ground potential due to current surges.

Vdd and Vbias are capacitively bypassed to Vss through 40 microfarads. Copper wire is use on Vdd and stainless steel micro-coaxial wire is used on Vbias. The shield for Vbias is tied to the ground plane of the clock interface and bias board but it is floated inside the dewar at the focal plane circuit card. The source lines are wired in a similar fashion with the shields only tied to the preamplifier board ground plane. This method of shielding ensures that no induced currents can flow on the shields.

All the electronics including the power supplies, the drive and data acquisition electronics, and the focal plane are completely enclosed in a shield which is tied to earth ground at the power supplies. This shield is then coupled to the analog ground line at the ADC through 100 Ohms.

2.4. The drive, data acquisition, and data transmission electronics

To minimize development effort and cost, a set of camera electronics was purchased from a vendor. The electronics system is a Model 300 manufactured by Rapax Systems and Engineering of Honolulu, Hawaii. The system consists of five components: the dewar electronics; a power supply unit; a high speed data receiver; and two AT-bus boards, one to control the dewar electronics, and the other an image buffer/processor board.

The dewar electronics, as the name implies, attaches directly to the outside of the camera dewar on an insulating, plexiglass mounting plate. The electronic components are housed inside a 12 x 24 x 3 in. steel box, which is subdivided into four separate chambers. One compartment contains the timing generator board, and another the clock/bias interface board. A third chamber houses the pre-amplifier electronics, and the last chamber contains the analog to digital converter (ADC) and the high speed data transmitter. The physical locations of these subsystems are arranged so as to minimize the length of the electrical connections to the FPA. Printed circuit boards are implemented for all noise-sensitive circuits (all but the timing generator board). In addition, optical isolators are used throughout to minimize digital noise and to eliminate ground loop problems.

The timing generator board uses conventional TTL logic to produce the clock levels which, in conjunction with the interface board, are needed to drive the array. Its operation mode (e.g., reset enabled, single sampling, triple sampling, etc.) is controlled by commands from the controller board sitting in the control PC's bus. The TTL level signals generated by the timing board are fed to the clock/bias interface board which uses level switching analog switches to finally generate the FPA clocks. The interface board also supplies the necessary biases required by the array. For this purpose it utilizes a low noise precision voltage source and filtering circuits.

The pre-amplifier board consists of four individual pre-amplifier channels, one for each of the four NICMOS3 outputs. Each channel provides its own current source load for each of the NICMOS3 output MOSFETs, a DC offset compensation circuit, and a differential input stage. The four channels are sequentially multiplexed to a buffer amplifier which in turn connects to the ADC board. The ADC board filters the signal using two passive high pass filters and then digitizes it to 16 bits in 2 μsec. The overall resolution of this signal chain is 22.20 μV/digital number (DN), with a noise performance of

approximately 35 μV rms. The digitized data is then serialized and transmitted through two coaxial cables to the data receiver unit. The serialization and transmission process is accomplished by a pair of "Transmitter Transparent Asynchronous Xmitter-Receiver Interface" (TAXI) ICs which take as input the 16-bit data from the ADC.

At the receiving end, the high speed data receiver, which consists primarily of a set of TAXI receiver ICs, translates the serialized data to parallel format and feeds it to the buffer/processor board inside the PC. The buffer board has enough 32-bit wide memory to store up to two separate 256 x 256 pixel images. Processor circuitry is present to allow various on-the-fly operations such as coaddition, background subtraction, and correlated multiple sampling. In addition, the board also possesses various counters which are used to provide the time measurement for integrations independently of the PC.

2.5. The image acquisition and analysis software

As mentioned earlier, while operating at the telescope the PC is slaved to the telescope computer. In this mode, the PC operates with a subset of the total software, which allows it to command the camera based upon instructions specified from the telescope computer via an ethernet link. The astronomers using PFIRCAM perform most of their analysis with IRAF or other software packages intended for image processing of astronomical data.

On the other hand, for the purpose of testing and characterization at the laboratory, a sophisticated software package has been specifically developed. The code has been written in C++ to insure modularity and ease of expandability. In order to have full access to PC memory, and also to provide an user friendly interface, the code has been targeted to operate under MS Windows. (Currently plans are under way to upgrade the code to the 32-bit programming environment of MS Windows NT). A typical screen is illustrated in Fig. 3.

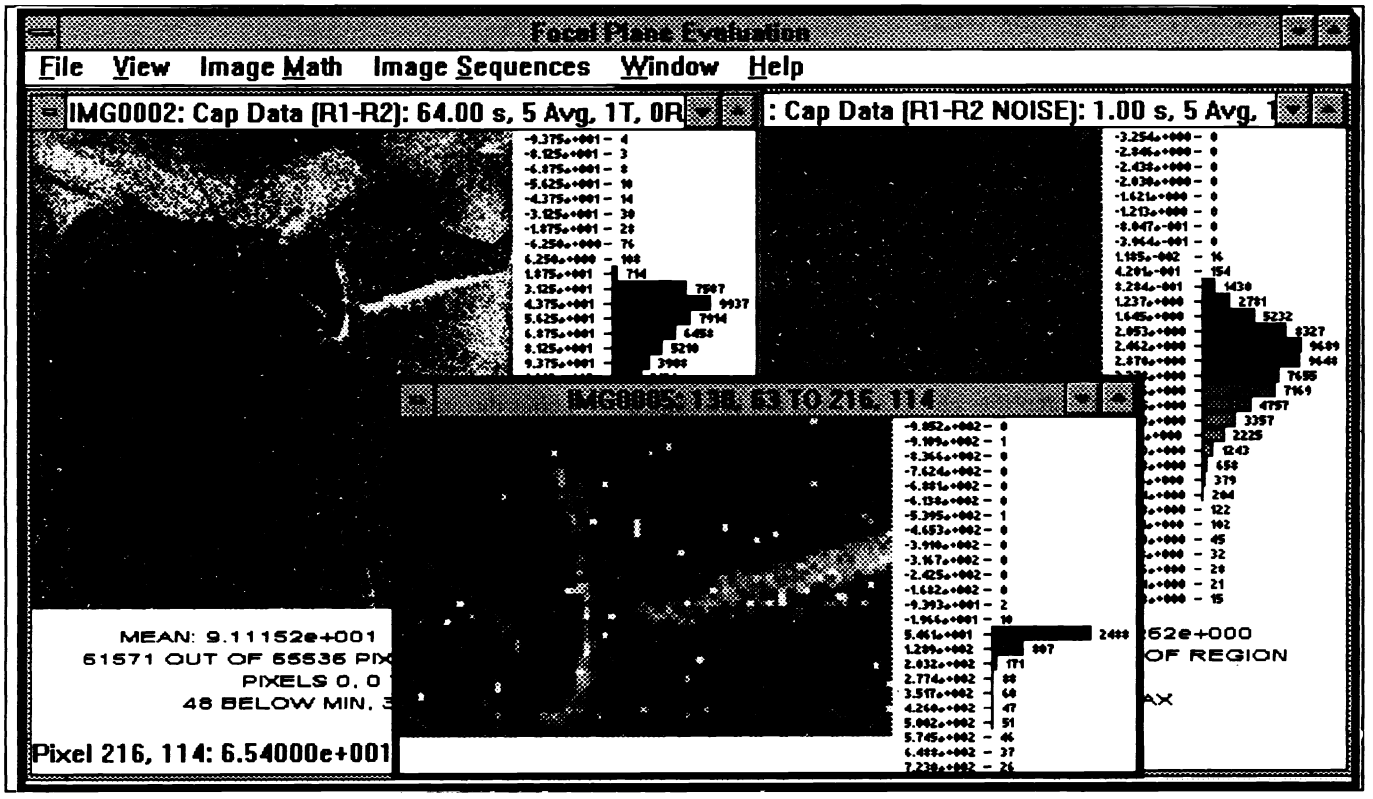

Figure 3. Illustration showing a typical screen from the array analysis software.

The software has been developed as a general laboratory tool, not specific to the PFIRCAM. Its modular structure allows for straight forward modifications to accommodate an altogether different system. Various data acquisition systems can be incorporated by modifying a single module of code, the data acquisition object. The image analysis and display part of the

code has been written to handle, without code modification, any array configuration possible from line arrays to 1024 x 1024 or larger formats.

The FPA analysis routines implemented into the software so far include measurements of parameters such as responsivity, spatial uniformity, temporal noise on a pixel-to-pixel basis, linearity, dark current, drift/stability, integration node capacitance, and multiplexer gain. The specific procedures for making these measurements will be discussed with the FPA analysis data presented in the sections that follow. Other significant analysis capabilities of the software include least squares fitting to various data formats, array image arithmetic, image sub-region analysis (i.e., any of the functions listed so far can be performed on selected sub-regions of the array). The image data can be displayed in various formats such as pixel maps of the whole array or of selected sub-regions, XY plots for selected pixels as a function of an user specified parameter, and histograms. There is also a continuous display mode useful to monitor time-dependent system variations, and while observing, it can be used to focus the telescope. Lastly, the software features a mode in which the user can specify a sequence of data acquisition and simple analysis commands in a file. This allows for time consuming and tedious data acquisition sequences to be fully automated.

3. NICMOS3 FPA CHARACTERIZATION AND EVALUATION

In what follows we present characterization and evaluation data on the NICMOS3 array currently being used in the system. Performance data specific to the electronics has been presented in an earlier publication[5].

3.1. Integration node capacitance and multiplexer gain

Before any performance parameters can be measured for a FPA, it is first necessary to determine its response in terms electrons per volt; i.e., the number of electrons generated at the pixel active cell per volt measured at the multiplexer's output amplifier. In equation form this is summarized by:

$$V_s = \frac{qN}{C_{\text{int}}(V)} G_{mux} \qquad \text{(Eq. 1)}$$

where V_s is the voltage measured at the multiplexer's output amplifier, q is the Coulomb constant, N is the number of electrons generated at the pixel, G_{mux} is the combined gain of the unit cell source follower and the output amplifier source follower, and $C_{\text{int}}(V)$ is the integration node capacitance described in section 1. G_{mux} can be determined by varying the reset voltage (DET BIAS, of Fig. 1) in 0.1 V steps and measuring the resulting voltage at the output amplifier (V_s). The slope of the curve generated by plotting V_s as a function of DET BIAS is G_{mux}. Fig. 4 displays the mean value of V_s for all pixels of the array vs. DET BIAS. The curve shows to be very linear within the normal DET BIAS operating range, with a mean value for G_{mux} of 0.988.

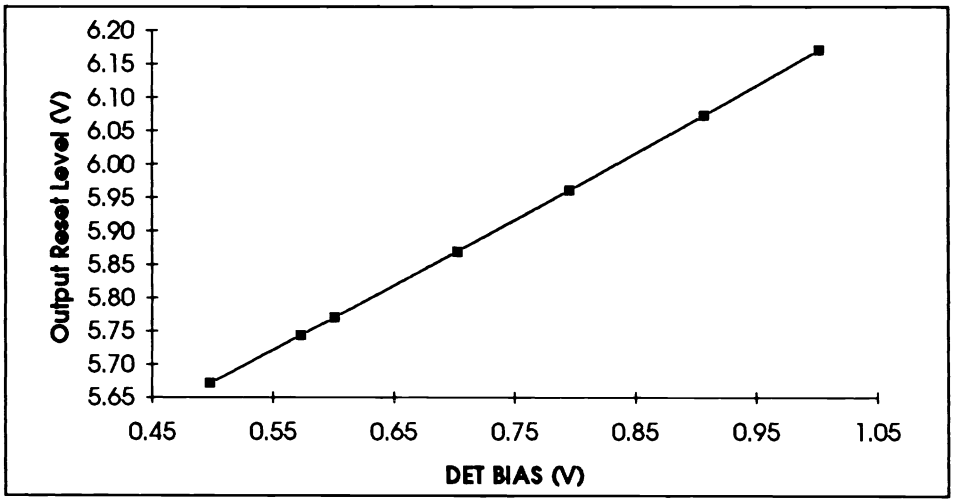

Figure 4. Reset level at the output amplifier vs. DET BIAS. The slope gives the multiplexer combined gain.

The measurement of C_{int} is a little more involved. First of all the camera must be made to view an uniform source. A sequence of signal frames, together with their corresponding noise frames, are then collected for increasing integration times. The starting integration time is chosen to be long enough so that the signal frames are shot noise limited. For this case the noise V_n is given by:

$$\langle V_n \rangle = \frac{q\sqrt{N}}{C_{int}} G_{mux} \qquad \text{(Eq. 2)}$$

Thus, the integration node capacitance C_{int} can be calculated for each pixel by taking the ratio of the frame signals to their shot noise squared and then scaling by the Coulomb constant and correcting for the multiplexer gain:

$$C_{int} = \frac{qV_s}{\langle V_n \rangle^2} G_{mux} \qquad \text{(Eq. 3)}$$

The mean value of C_{int} obtained by this approach was 0.08 pF. This value combined with G_{mux} and the signal chain resolution of 22.20 μV/DN (section 2.4) results in an overall system resolution of 11 electrons/DN.

3.2. FPA read noise

The read noise for the array is determined by calculating, on a pixel-by-pixel basis, the rms deviations from the mean signal of a sequence of dark frames all having identical collection parameters. Fig. 5 shows a pixel map and histogram for the read noise calculated from 30 averaged dark frames with a short integration time. The read noise mean value for the array is 33.0 electrons, with lowest noise observed in quadrant 4, as can be seen in Fig. 5.

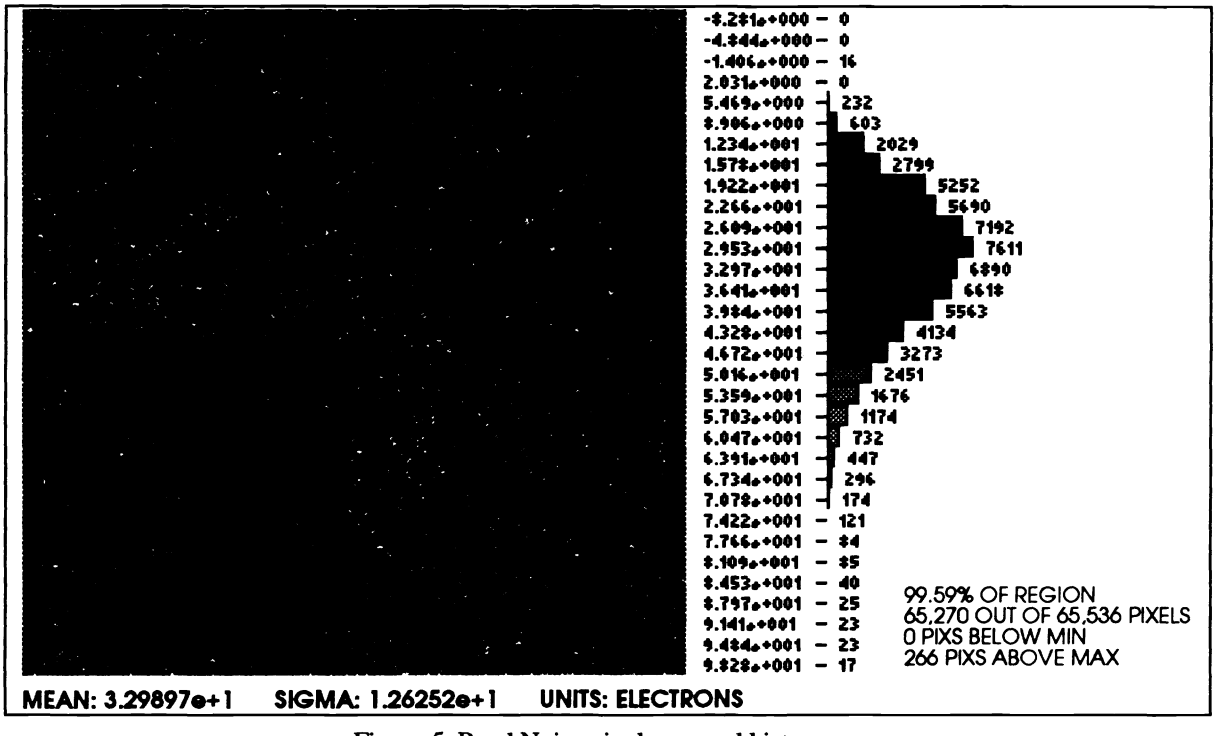

Figure 5. Read Noise pixel map and histogram.

3.3. Dark current

Fig. 6 shows the dark current calculated from the average of ten 120 sec dark frames. A mean dark current of 17.4 e-/s was measured for the whole array. Variations in this number are readily apparent from the pixel map, with the center of the

array and the lower left quadrant (quadrant 4) showing the lowest dark current (approximately 9 e-/s). These numbers are significantly higher than would be expected for photodiodes with resistance-area products (R_oA) as large as 10^{13} Ω-cm^2, such as those found in the NICMOS3,[6] which are expected to exhibit dark currents of only a few electrons per second. This leads us to conclude that some 300 K photons are leaking through the shielding to the detector.

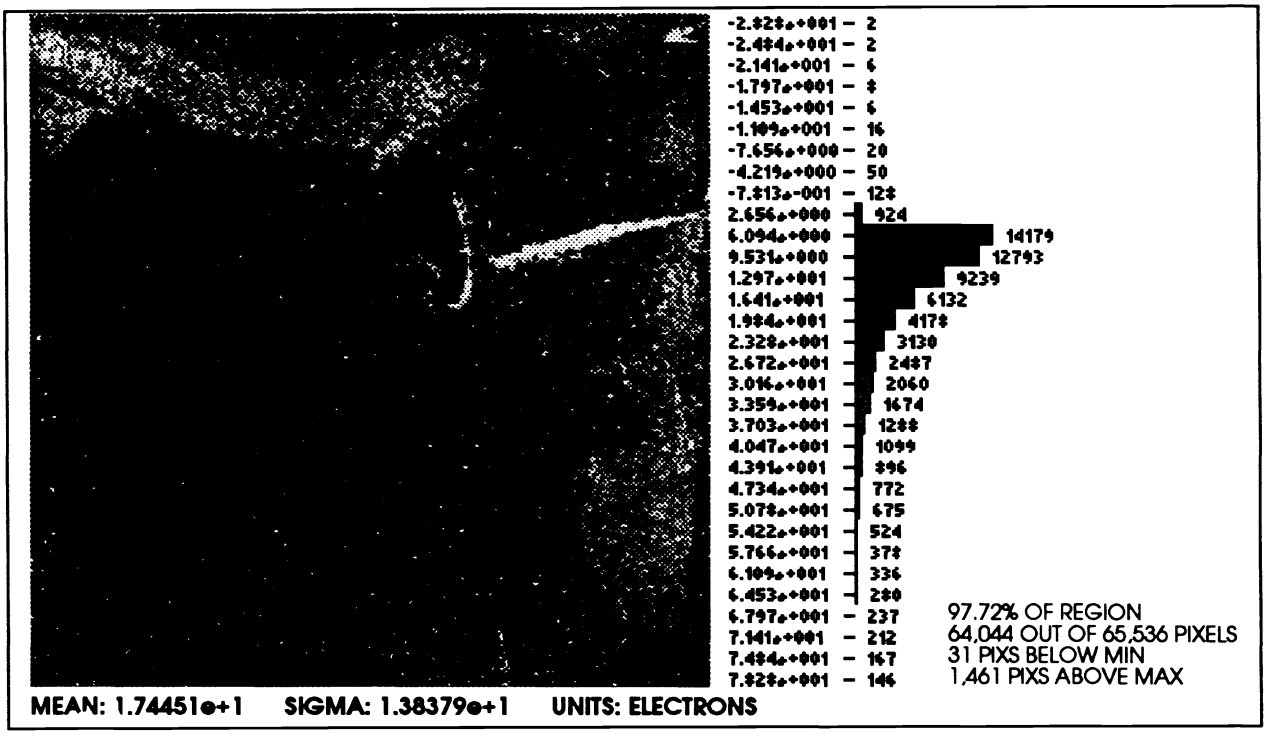

Fig. 6. Dark current map and histogram.

3.4. Electroluminescence

Another source of dark signal, besides the dark current, is the electroluminescence of the output amplifier MOSFETs. Fig. 7 shows the location and extent of the glowing amplifiers. Fortunately, the magnitude of the glow is not integration time dependent, provided the amplifiers are off when integrating, and therefore can be easily subtracted from image data. At a worst case we have observed the magnitude of the glow to be approximately a couple of hundred electrons over the dark current signal.

3.5. Linearity analysis

As part of the calibration of the system, a detailed characterization of the array's responsivity non-linearity has been carried out. The procedure involves acquiring a sequence of signal frames for various increasing integration intervals, up to the point were the array saturates. The camera is made to view an uniform source (e.g., the telescope mirror cover) and a narrow-band filter is used to ensure that the array does not saturate too quickly. A least squares fit to a second order polynomial is then performed on the data and coefficients are calculated on a pixel-to-pixel basis to satisfy the equation:

$$S_i = A0_i + A1_i\tau + A2_i\tau^2 \qquad \text{(Eq. 4)}$$

where S_i is the signal level of the ith pixel, τ is the integration time, $A0_i$ is the DC offset for that pixel, $A1_i$ is a measure of the responsivity of the pixel in units of DN/s or e/s, and $A2_i$ is a measure of the non-linearity of the pixel in units of DN/s^2 or e-/s^2.

The results from this analysis can be seen in Fig. 8, both as pixel maps and histograms. Fig. 8a displays coefficient *A*0 in units of DN having a fairly uniform distribution throughout the array and a nicely symmetric histogram. The pixel map of *A*1 (Fig. 8b) is not as uniform, showing the most sensitive pixels (whitest ones) to be in a cloud pattern covering most of quadrant 4 and the center of the array. Finally Fig. 8c depicts the non-linear behavior of the array, with the pixels most deviant from linearity (whitest ones) located towards the right edge of the array, covering large portions of quadrant 2, and to a lesser extent, quadrant 3.

From the linearity data it is also possible to determine the useful dynamic range for each pixel. This is calculated by determining the signal level for which the pixel begins to saturate and becomes extremely non-linear. Fig. 9 presents the results of this calculation as a pixel map and a histogram with units of DN. Interestingly, quadrant boundaries are very apparent in the pixel map, which depicts whitest pixels as having the largest dynamic ranges. A mean dynamic range for the array of 13,700 DN or 150,700 e- can be estimated from the histogram. This number is in disagreement with the expected full well capacity of 250,000 e- for a 0.5 V operating reverse-bias. Part of the missing dynamic range can be accounted by our particular mode of readout scheme. For the purpose of improving noise performance, it involves acquiring a small number of 'settling' frames after the reset and before the integration begins. However, this only accounts for a small portion of the loss.

3.6. Reset anomaly

A significant part of the dynamic range is being lost immediately after resetting the array by clock feed-through and/or some kind of charge injection mechanism. We have measured the amount of charge being fed into the integration node by subtracting from a reset frame the signal frame read immediately after it. An average of several 'reset-read' subtractions is shown in Fig. 10 for quadrant 1 of the array. Here we see that an average of 59,400 e- are making their way into the integration node after reset, a rather significant portion of the dynamic range. In addition, the noise measured in this readout scheme showed to be quite consistent with the expected KTC noise, indicating that the amount of charge injected into the integration node is fairly constant every time the array is readout.

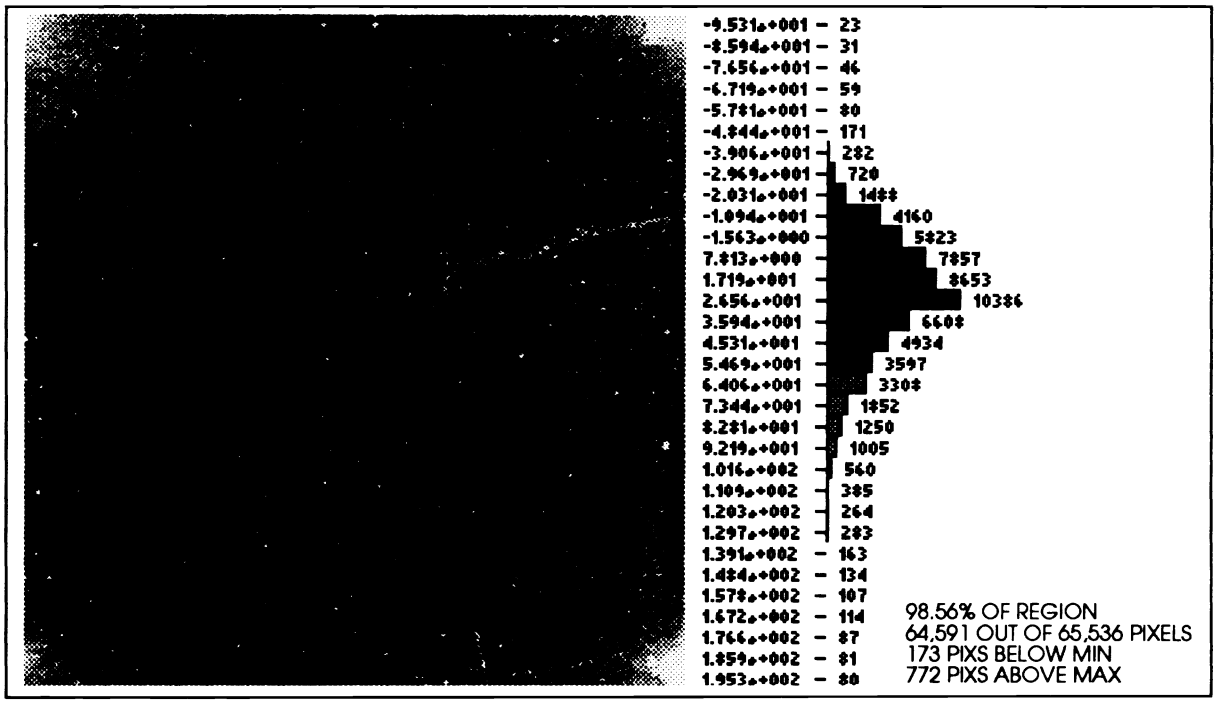

Fig. 7. Output amplifier glow.

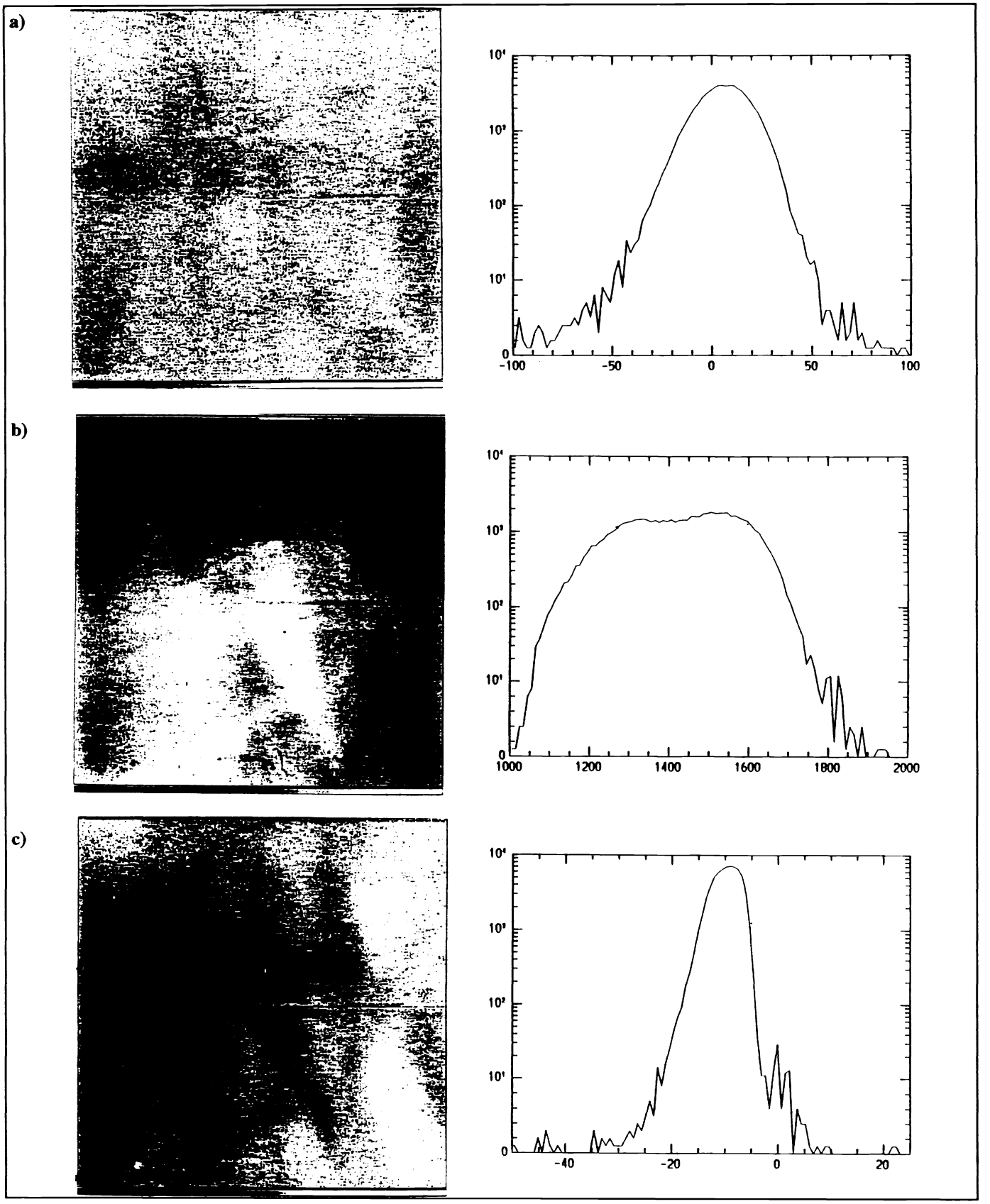

Figure 8. Linearity coefficients (a) A0, (b) A1, and (c) A2.

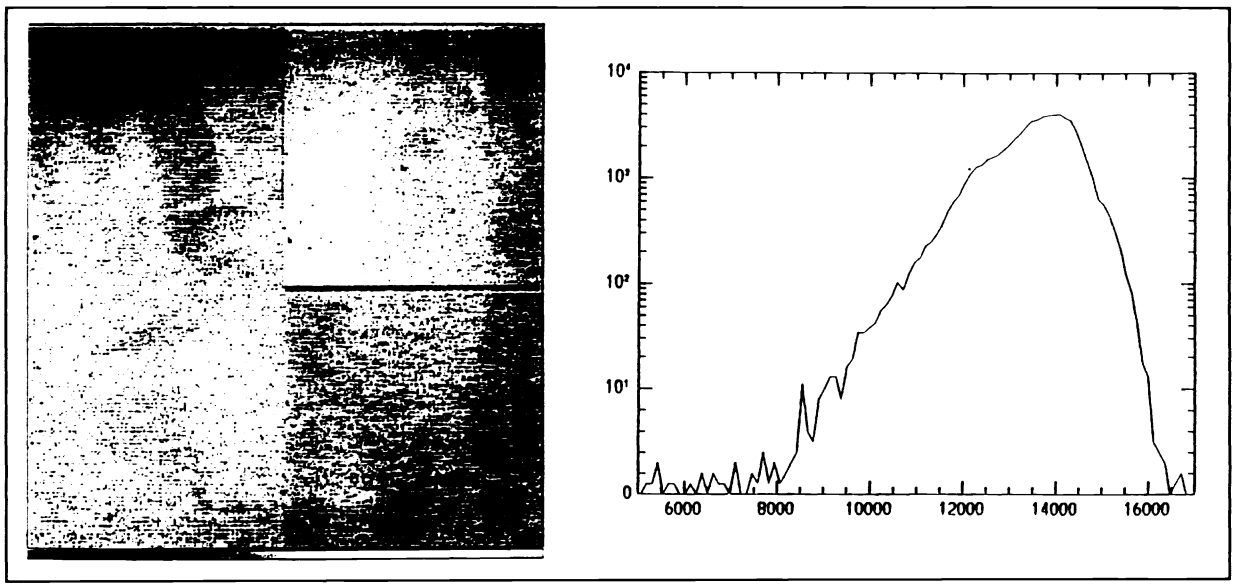

Figure 9. Dynamic Range (DN).

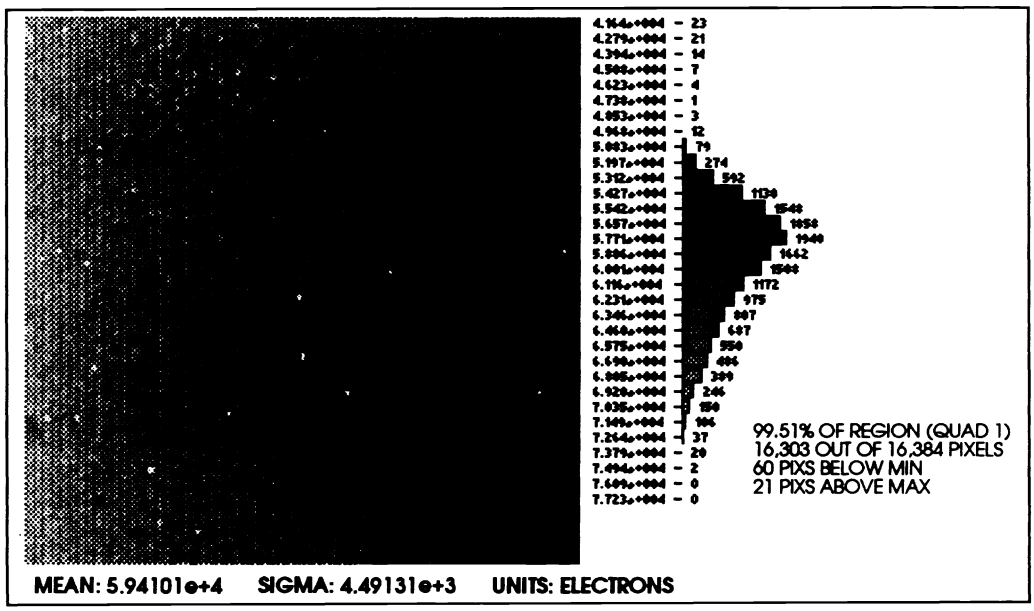

Figure 10. Reset Anomaly.

4. OBSERVING DATA AT MT. PALOMAR

To end we would like to present some of the data that this camera has acquired at the 200" telescope. Fig. 11 is a K-band (2.2 μm) image of the Ring Nebula (M57). Fig. 12 is a mosaic of various frames taken near the far-infrared source 03282+3035, which is located roughly near the center of the image. The image shows a collimated jet of molecular hydrogen emission (2.12 μm H_2 (1-0)) whose origin is via shock-excited gas (Herbig-Haro phenomenon) associated with the energetic molecular outflow. Finally Fig. 13 shows a collection of three images of NGC 4713. The top left image was taken through a narrow-band filter centered on the Brackett gamma emission line (Br. γ + Continuum), the top right was collected through a narrow-band filter slightly offset from Br. γ (Continuum), and the bottom image was generated by subtracting the previous two images to reveal the Br. γ sources.

Figure 11. K-band image of the Ring nebula.

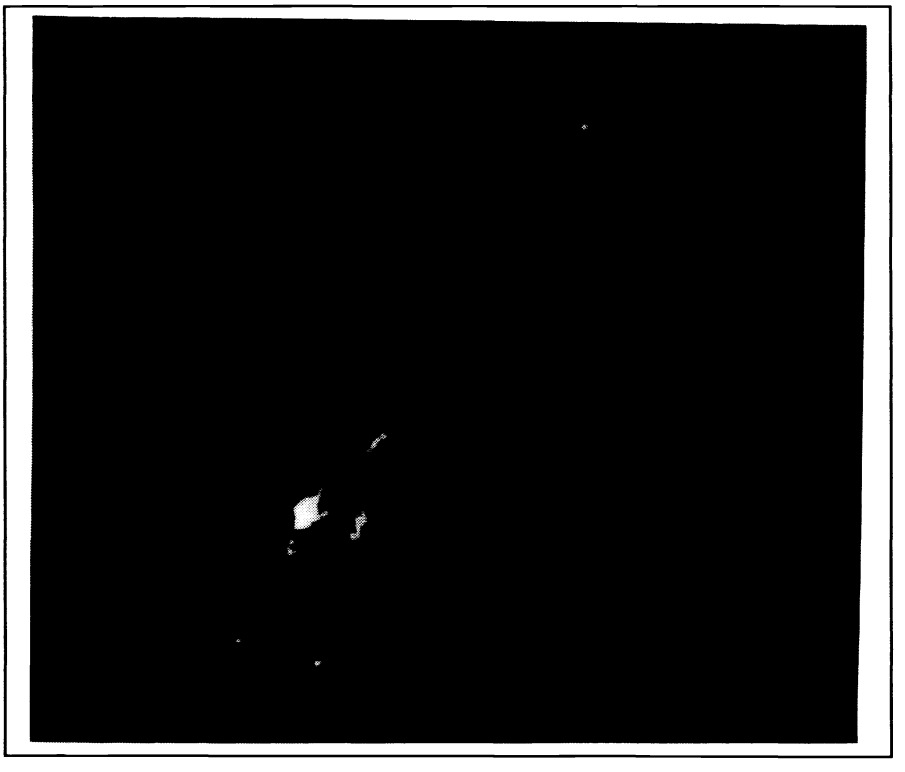

Figure 12. 2.12 μm H2 (1-0) image near the IRAS far-infrared source 03282+3035.

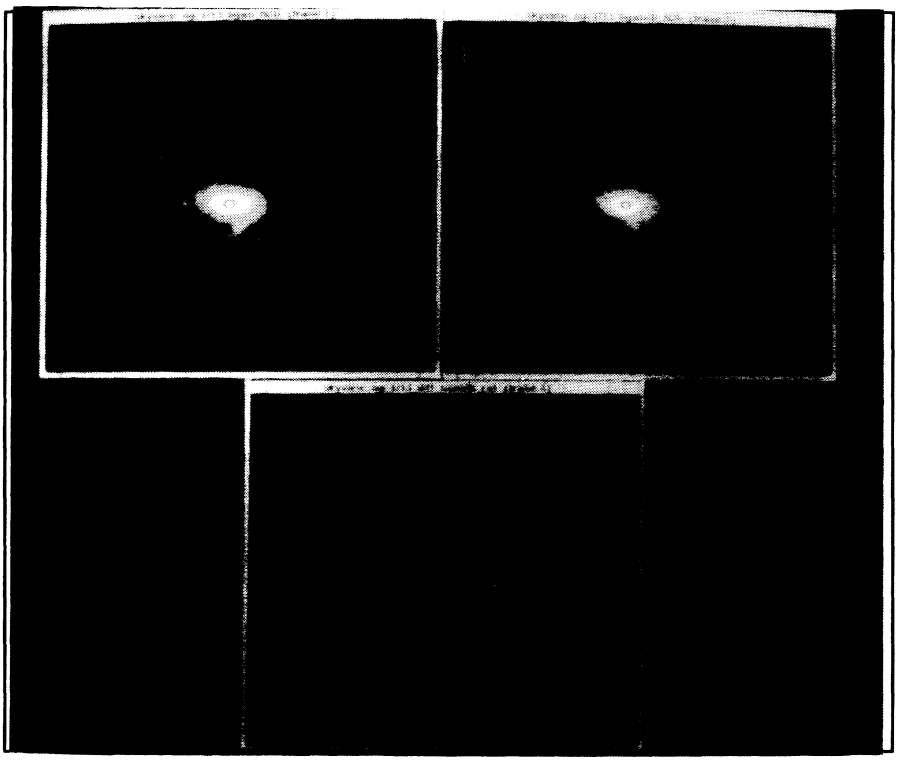

Figure 13. Brackett γ + Continuum, Continuum, and Brackett γ images of NGC 4713.

5. ACKNOWLEDGMENTS

The research described in this paper was carried out by the Jet Propulsion Laboratory, California Institute of Technology, under a contract with the National Aeronautics and Space Administration.

Reference herein to any specific commercial product, process, or service by trade name, trademark, manufacturer, or otherwise, does not constitute or imply its endorsement by the United States Government or the Jet Propulsion Laboratory, California Institute of Technology.

6. REFERENCES

[1]C. Bruce, C. Beichman, D. Van Buren, N. Gautier, C. Jorquera, K. Seaman, "Development and test of an IR camera for astronomical observation at the Palomar 200-in. Observatory using the NICMOS II Array," *Proc. SPIE*, Vol. 1762, pp. 444-460 (1992).

[2]K. Vural, L. J. Kozlowski, J. K. Chen, B. Bailey, D. Bui, R. Thompson, R. Rasche, M. Rieke, and B. Kleinhans, "SWIR 256x256 and 128x128 PACE-1 PV HgCdTe Focal Plane Arrays for the Near-Infrared Camera and Multi-Object Spectrometer (NICMOS)," *Proceedings of the 1990 Infrared Detector Technology Meeting*, National Institute of Standards and Technology (1990).

[3]J. L. Schmit and F. L. Stelzer, "Temperature and Alloy Compositional Dependencies of the Energy Gap of $Hg_{1-x}Cd_xTe$," *J. Appl. Phys.*, Vol. 40, No. 12, pp. 4865-4869 (1969).

[4]F. E. Ross, "Lens systems for the correction of coma in mirrors," *Astrophys J.*, Vol. 81, No. 1, pp. 156-172 (1935).

[5]Ref. 1.

[6]Ref. 2.